



**Environmental  
Science**  
Nano

**Discovery and potential ramifications of reduced iron oxide nanomaterials—magnetite, wüstite, and zero-valent iron—in wildland-urban interface fire ashes**

Journal:	<i>Environmental Science: Nano</i>
Manuscript ID	EN-ART-05-2022-000439.R1
Article Type:	Paper

**SCHOLARONE™**  
Manuscripts

## Environmental Significance

Fires at the wildland-urban interface have been increasing in frequency, size, and severity, resulting in increased emissions of contaminants, including incidental nanomaterials. This study reports the speciation and concentrations of iron-bearing nanomaterials in wildland-urban interface ashes. Maghemite and magnetite were detected in most ashes and accounted for 0-90 and 0-81% of the spectral weight, respectively. Ferrihydrite, goethite, and hematite were identified less frequently in ashes than maghemite and magnetite and accounted for 0-65, 0-54, and 0-50% of spectral weight, respectively. Other iron phases identified in ashes include wüstite, zerovalent iron, FeS, FeCl<sub>2</sub>, FeCl<sub>3</sub>, FeSO<sub>4</sub>, Fe<sub>2</sub>(SO<sub>4</sub>)<sub>3</sub>, and Fe(NO<sub>3</sub>)<sub>3</sub>. These findings suggest that fires convert iron oxides (*e.g.*, maghemite, hematite, and goethite) to reduced iron phases such as magnetite, wüstite, and zerovalent iron. Such transformation of iron phases can have serious environmental and human health effects as magnetite nanomaterials have been linked to neurodegenerative diseases as well as climate change.

1  
2  
3 **Discovery and potential ramifications of reduced iron oxide nanomaterials—magnetite,**  
4 **wüstite, and zero-valent iron—in wildland-urban interface fire ashes**  
5  
6  
7  
8  
9

10 Mohammed Baalousha<sup>1\*</sup>, Morgane Desmau<sup>2</sup>, Sheri Singerling<sup>3</sup>, Jackson P. Webster<sup>4</sup>, Sandrine J.  
11  
12 Matiasek<sup>5</sup>, Michelle A. Stern<sup>6</sup>, and Charles N. Alpers<sup>6</sup>  
13  
14  
15  
16

17 <sup>1</sup> Center for Environmental Nanoscience and Risk, Department of Environmental Health Sciences,  
18  
19 Arnold School of Public Health, University of South Carolina, Columbia, South Carolina, United  
20  
21 States  
22

23  
24 <sup>2</sup> Deutsches Elektronen-Synchrotron DESY, Notkestr. 85, 22607 Hamburg, Germany  
25

26  
27 <sup>3</sup> NanoEarth, Institute for Critical Technology and Applied Science, Virginia Polytechnic Institute  
28  
29 and State University, Blacksburg, Virginia, United States  
30

31  
32 <sup>4</sup> Department of Civil Engineering, California State University Chico, 400 W 1<sup>st</sup> St, Chico, CA  
33  
34 95929, United States  
35

36  
37 <sup>5</sup> Department of Earth and Environmental Sciences, California State University Chico, 400 W 1<sup>st</sup>  
38  
39 St, Chico, CA 95929, United States  
40

41  
42 <sup>6</sup> U.S. Geological Survey, California Water Science Center, 6000 J Street, Sacramento, CA 95819,  
43  
44 United States  
45  
46

47 \* Corresponding author: [mbaalous@mailbox.sc.edu](mailto:mbaalous@mailbox.sc.edu)  
48  
49  
50  
51  
52  
53  
54  
55  
56  
57

## Abstract

The increase in fires at the wildland-urban interface has raised concerns about the potential environmental impact of ash remaining after burning. Here, we examined the concentrations and speciation of iron-bearing nanoparticles in wildland-urban interface ash. Total iron concentrations in ash varied between 4 and 66 mg g<sup>-1</sup>. Synchrotron X-ray absorption near-edge structure (XANES) spectroscopy of bulk ash samples was used to quantify the relative abundance of major Fe phases, which were corroborated by transmission electron microscopy measurements. Maghemite ( $\gamma$ - (Fe<sup>3+</sup>)<sub>2</sub>O<sub>3</sub>) and magnetite ( $\gamma$ - Fe<sup>2+</sup>(Fe<sup>3+</sup>)<sub>2</sub>O<sub>4</sub>) were detected in most ashes and accounted for 0-90 and 0-81% of the spectral weight, respectively. Ferrihydrite (amorphous Fe(III)-hydroxide, (Fe<sup>3+</sup>)<sub>5</sub>HO<sub>8</sub>.4H<sub>2</sub>O), goethite ( $\alpha$ -Fe<sup>3+</sup>OOH), and hematite ( $\alpha$ - Fe<sup>3+</sup><sub>2</sub>O<sub>3</sub>) were identified less frequently in ashes than maghemite and magnetite and accounted for 0-65, 0-54, and 0-50% of spectral weight, respectively. Other iron phases identified in ashes include wüstite (Fe<sup>2+</sup>O), zerovalent iron, FeS, FeCl<sub>2</sub>, FeCl<sub>3</sub>, FeSO<sub>4</sub>, Fe<sub>2</sub>(SO<sub>4</sub>)<sub>3</sub>, and Fe(NO<sub>3</sub>)<sub>3</sub>. Our findings demonstrate the impact of fires at the wildland-urban interface on iron speciation; that is, fires can convert iron oxides (*e.g.*, maghemite, hematite, and goethite) to reduced iron phases such as magnetite, wüstite, and zerovalent iron. Magnetite concentrations (*e.g.*, up to 25 mg g<sup>-1</sup>) decreased from black to gray to white ashes. Based on transmission electron microscopy (TEM) analyses, most of the magnetite nanoparticles were less than 500 nm in size, although larger particles were identified. Magnetite nanoparticles have been linked to neurodegenerative diseases as well as climate change. This study provides important information for understanding the potential environmental impacts of fires at the wildland-urban interface, which are currently poorly understood.

## 1. Introduction

Fire is a natural process that has occurred in many ecosystems worldwide since the evolution of land plants some 250 to 400 million years ago<sup>7</sup>. The crux of the wildfire problem nowadays is the increased fire frequency, size, severity<sup>8</sup>, and the spread of fires into the built environment (*i.e.*, fires at the wildland-urban interface, WUI), resulting in increased emissions of contaminants of emerging concern<sup>9, 10</sup>, many of which remain to be discovered. Both known and unknown contaminants from fires threaten ecosystems with implications for air and water pollution and, subsequently, environmental and human health<sup>11, 12</sup>. For instance, particulate matter from wildfires is more toxic than equal doses from other sources such as ambient pollution<sup>13, 14</sup>. Wildfire smoke impacts respiratory health more than fine particles from other sources<sup>15, 16</sup>. Additionally, recent studies have found an association between wildfires and wood smoke exposure to cognitive dysfunction, including Alzheimer's disease and dementia<sup>17, 18</sup>, yet it is not clear which contaminants in the wildfire emissions contribute to this disease.

Fire at the WUI transforms fuels (*i.e.*, vegetation, soil organic matter, and construction material) into materials with different chemical and physical properties, including black carbon, methane, carbon monoxide, carbon dioxide and ash<sup>1</sup>. These fire emissions (*e.g.*, black carbon, methane, carbon monoxide) together with the heat generated by the fires render the surrounding environment highly reductive<sup>2, 3</sup>. For instance, previous studies demonstrated the reduction of TiO<sub>2</sub> to titanium suboxides (*e.g.*, Magnéli phases) in coal burning power plants<sup>4, 5</sup>. Ash is the particulate residue after fire that remains in situ, is transported in air, or is deposited on the ground, and consists of minerals and charred organic materials<sup>1</sup>. The quantity and characteristics of ash produced during a fire depend on fuel type, combustion completeness, and burned fuel. Low combustion completeness (low fire severity, *e.g.*, T < 450 °C) forms black ash with organic carbon

1  
2  
3 as the main component. At high combustion completeness (high fire severity, *e.g.*,  $T > 450$  °C),  
4  
5 most organic carbon is volatilized, leaving behind mineral ash (or white ash) with calcium,  
6  
7 magnesium, sodium, potassium, silicon, and phosphorus in the form of inorganic minerals, mostly  
8  
9 carbonates <sup>19-21</sup>. At combustion temperatures  $> 850$  °C, the most common inorganics are oxides,  
10  
11 including iron oxides <sup>1</sup>.

12  
13  
14 In plants, among the various organic Fe compounds, the protein phytoferritin stores iron as  
15  
16 a hydrous ferric hydroxide similar to ferrihydrite ( $(\text{Fe}^{3+})_5\text{O}_8 \cdot 4\text{H}_2\text{O}$ ) <sup>22,23</sup>, which may contribute to  
17  
18 pedogenic Fe mineral assemblages in soils <sup>24,25</sup>. Iron stored in ferritin and other organic materials  
19  
20 could potentially transform to ferromagnetic phases during the burning of plant material. In man-  
21  
22 made structures, iron oxides are widely used as pigment in paints, coatings, and construction  
23  
24 material such as concrete products, mortar, paving stones, and roofing tiles. Iron oxide pigments  
25  
26 are used as colorants for ceramic glazes, glass, paper, plastic, rubber, and textiles as well as in  
27  
28 cosmetics and magnetic ink toner <sup>26</sup>. The total consumption of iron oxide pigments in the United  
29  
30 States was approximately 200,000 tons in 2020 <sup>27</sup>. Iron<sup>3+</sup> oxides and hydroxides (*e.g.*, hematite,  
31  
32 goethite, and to a lesser degree lepidocrocite) are the most widely used as pigments (*i.e.*, yellow,  
33  
34 orange, red, red purplish, and brown) <sup>28</sup>. Black pigment uses the mixed Fe<sup>2+</sup>/Fe<sup>3+</sup> oxide magnetite  
35  
36  
37  
38  
39  
40  
41  
42  
43  
44  
45  
46  
47  
48  
49  
50  
51  
52  
53  
54  
55  
56  
57  
58  
59  
60

41  
42 The combustion of vegetation and structural materials alters the speciation of iron oxides and  
43  
44 appears to lead to the formation of magnetite particles. A recent study demonstrated the magnetic  
45  
46 properties of plant ashes, which result from the thermal transformation of Fe in both organic and  
47  
48 inorganic particulate matter <sup>29</sup>. Another study demonstrated the presence of magnetite ( $\gamma$ -  
49  
50  $\text{Fe}^{2+}(\text{Fe}^{3+})_2\text{O}_4$ ) and/or maghemite ( $\gamma$ -  $(\text{Fe}^{3+})_2\text{O}_3$ ) particles in burned soils and plants characterized  
51  
52 by spherical shapes and sizes typically between 0.1 and 2  $\mu\text{m}$  <sup>30</sup>. The degree of pyrogenic magnetic  
53  
54  
55  
56  
57  
58  
59  
60

1  
2  
3 enhancement of fire-affected soils is strongly related to the wildfire severity. The highest  
4  
5 pyrogenic magnetic enhancement is linked to the occurrence of higher severity wildfires in pine  
6  
7 forests and is dominated by a superparamagnetic fraction, whereas wildfires of lower severity  
8  
9 cause lower pyrogenic enhancement with a larger relative contribution of single-domain  
10  
11 ferrimagnetic grains <sup>30</sup>.

12  
13  
14 Iron-bearing particles in fire ash, particularly magnetite, may have serious implications for  
15  
16 human health. Several studies have observed airborne magnetite nanoparticles (NPs) in different  
17  
18 human organs, suggesting that magnetite in the atmosphere may be able to enter the human  
19  
20 circulatory system or even the brain tissue <sup>31-33</sup>. Exposure of human lung cells to different  
21  
22 magnetite size fractions (including NPs) and doses revealed that the studied particles, although  
23  
24 being only slightly cytotoxic, led to increased reactive oxygen species formation, mitochondrial  
25  
26 damage, and genotoxic effects <sup>34</sup>. The presence of magnetite NPs in the brain is potentially  
27  
28 associated with several neurodegenerative diseases, including Alzheimer's and Parkinson's  
29  
30 diseases, and oxidative stress appears to play a key role in the pathogenesis of these diseases <sup>35, 36</sup>.  
31  
32 Additionally, magnetite NPs could have a host of environmental impacts, such as promoting the  
33  
34 formation of algal blooms <sup>37, 38</sup> as well as contributing to climate change from absorption of solar  
35  
36 radiation <sup>39, 40</sup>.

37  
38  
39  
40  
41  
42 Considering the potential health and global climate effects of magnetite particles, it is  
43  
44 important to better understand the emission levels and characteristics of magnetite particles from  
45  
46 fire emissions at the WUI. In this study, we assess the speciation of iron in ash generated by fires  
47  
48 at the WUI. Notably, as an emerging class of particulate pollutants, there have been no previous  
49  
50 reports on the occurrence of anthropogenic magnetite particles in WUI fire emissions. Therefore,  
51  
52  
53  
54  
55  
56  
57  
58  
59  
60

our results provide important information for understanding the pollution characteristics and health risks of magnetite particles generated from fires at the WUI.

## 2. Materials and methods

### 2.1. Sampling sites

Two wildland-urban interface fire sites that burned during the 2020 California fire season were examined in this study including the North Complex (NC) Fire, also known as the Bear Fire or the Claremont-Bear Fire and the LNU Lightning Complex Fire (**Figure 1**).

**North Complex (NC) Fire:** This fire, the seventh largest in California history and the second largest recorded in the northern Sierra Nevada, burned 1,290 km<sup>2</sup> and destroyed 2,455 structures in the Feather River watershed northeast of Lake Oroville, California, between August 17 and December 3, 2020. Lake Oroville is the largest reservoir of the California State Water Project, providing drinking water for more than 23 million of the state's 39 million residents. The West Zone of the fire consisted of 342 km<sup>2</sup> located primarily within the Plumas National Forest. Within the fire perimeter, the distribution of burn severity was 2% low, 8% moderate, and 89% high (**Figure 1a**)<sup>41, 42</sup>. The land use within the burned area was 84% evergreen forest, 12% shrub/scrub, and the elevation averaged 1,153 m and ranged from 260 to 2,132 m (**Figure S1**). The NC Fire burned 28% of the Middle Fork Feather River and 8% of the North Fork Feather River watersheds.

Fire ash and soil samples were collected in the Berry Creek community, where most of the structures were destroyed (**Table S1, Figure S1**). The general setting reflects much of the western slope of the Sierra Nevada in California in the 300-750 m elevation range in terms of geology and vegetation. The area is characterized by steep terrain underlain by granitic and metavolcanic bedrock. The soils vary based on the underlying parent formations with granite forming decomposed granite soil in some areas and the metavolcanic rocks forming "red dirt" soils



1  
2  
3 including the Hartsmill series. At lower elevations ca. 300 m, vegetation is characterized by  
4 manzanita (*Arctostaphylos spp.*), toyon (*Heteromeles arbutifolia*), interior live oak (*Quercus*  
5 *wislizeni*), California black oak (*Quercus kelloggii*), Pacific poison oak (*Toxicodendron*  
6 *diversilobum*) and very scattered ponderosa pine (*Pinus ponderosa*). At higher elevations ca. 750  
7  
8 m, vegetation cover is characterized by California mixed conifers including black and live oaks,  
9  
10 Pacific madrone (*Arbutus menziesii*), ponderosa pine, Douglas-fir (*Pseudotsuga menziesii*), and  
11  
12 mixed shrub species.  
13  
14  
15  
16  
17  
18

19 ***The LNU Lightning Complex Fire:*** This fire, the sixth largest in California history, burned  
20  
21 1,470 km<sup>2</sup> and destroyed 1,491 structures in Colusa, Lake, Napa, Sonoma, Solano, and Yolo  
22  
23 Counties, approximately 60 km west of Sacramento, between August 17 and October 2, 2020<sup>43</sup>.  
24  
25 Within the fire perimeter, the distribution of burn severity was 12% low, 39% moderate, and 49%  
26  
27 high (**Figure 1b**). Land use in the fire perimeter comprised of 57% shrub/scrub, 19% herbaceous,  
28  
29 12% evergreen forest, and 1.4% developed (**Figure S2**). Roughly half of the Upper Putah Creek  
30  
31 watershed was burned and 6.4, 5.5, 4.3, and 3.9% of the upper Cache Creek, Russian River, Suisun  
32  
33 Bay, and Lower Sacramento River watersheds burned, respectively. Elevation within the fire  
34  
35 footprint was on average 370 m and ranged between 40 and 930 m.  
36  
37  
38  
39

40 Fire ash samples were collected from vegetated areas and the built environment in Napa  
41  
42 and Solano Counties in the vicinity of Lake Berryessa (**Table S1, Figure S2**). The general setting  
43  
44 is typical of the Coast Ranges in central California. Elevation of valleys in the Lake Berryessa  
45  
46 region generally ranges from 90 to 120 m, with ridge elevations from 600 to 900 m. The geology  
47  
48 of the Lake Berryessa region has a diversity of rock types including deformed, metamorphosed  
49  
50 sedimentary and volcanic rocks of the Franciscan Complex; sedimentary and volcanic rocks of the  
51  
52 Great Valley sequence; igneous rocks of the Clear Lake Volcanics; and alluvium. Soils in the area  
53  
54  
55  
56  
57  
58  
59  
60

1  
2  
3 are typically well-drained and include the Henneke series, formed from weathered, ultramafic  
4 rocks such as serpentinite; the Forward series, formed from weathered volcanic rocks; and the  
5 Bressa series, formed from weathering of sandstone and shale. Vegetation is diverse in the Lake  
6 Berryessa region and varies by elevation. Valley floors typically have grasslands and valley oak  
7 woodlands with riparian habitats along creeks and streams; at middle elevations, hardwood forests  
8 have various oak species, gray pine, madrone, and chaparral; higher elevations support Douglas-  
9 fir, ponderosa pine, incense cedar (*Calocedrus decurrens*), and montane chaparral.

## 19 **2.2. Sample collection**

20  
21 Fifty-five ash and soil samples were collected during October-November 2020 in the two fire-  
22 affected areas (**Figure 1, Table S1**). In the LNU Lightning Complex Fire area, thirty-two ash  
23 samples were collected from burned structures and three samples from burned vegetation. In the  
24 North Complex area, nine ash samples were collected from burned structures and vehicles, five  
25 ash samples from burned vegetation, and six soils affected by fire. In addition, a sample of air-fall  
26 ash was collected from a car's windshield during the 2019 fire season. All samples were collected  
27 prior to any rain or other precipitation.

28  
29 The ash samples were collected from various sources including residential structures, garages,  
30 vehicles, vegetation, and soils representing low to high burn severity (**Table S1**). The burned  
31 structures included residences, a convenience store, and storage sheds; burned vehicles included  
32 automobiles, tractors, and a boat on a trailer. Vegetation types sampled included oak, pine,  
33 manzanita, chamise, and grasses.

34  
35 Within the LNU Lightning Complex Fire area, undisturbed ash samples were collected from  
36 burned structures and vegetation to represent specific location sources; ash samples were collected  
37 from multiple locations (*e.g.*, kitchen, living room, bedroom, garage, foundation, *etc.*) within each  
38 residential structure; detached structures adjacent to residences (*e.g.*, sheds, barns, and trailers) and

1  
2  
3 a commercial structure (convenience store) were also sampled (**Table S1**). Ash samples were  
4 collected with disposable plastic scoops and placed into zippered plastic bags.  
5  
6

7  
8 Within the NC Fire area, ash and soil samples (**Table S1**) were collected from around the  
9  
10 Madrone Lake Community. Undisturbed ash was scraped from the soil surface and collected to  
11 represent average (mixed) sources (**Figure S3**). In burned structures from the NC fire area, ash  
12 collected from multiple locations within the footprint of the structure was combined to form a  
13 representative composite sample. Note that sampling burned structures is very difficult because  
14 the ash is not uniform like vegetation ash. Structural ash often a mixture of wallboard, insulation,  
15 large debris, and combusted material residuals. To collect underlying soil, the area where surface  
16 ash was collected was cleared of additional ash and the underlying soil was collected using a plastic  
17 scoop from two soil depths (0-2 cm, NC 12B and NC 13B, and 10-15 cm, NC 12C and NC 13C).  
18 All samples were collected in acid-washed HDPE wide-mouth bottles.  
19  
20  
21  
22  
23  
24  
25  
26  
27  
28  
29

### 30 31 **2.3. Transmission Electron Microscopy**

32  
33 Transmission electron microscopy (TEM) was used to study the morphology, dimensions,  
34 crystallinity, and elemental composition of NPs in a select set of ash samples (A122 and A124).  
35 The samples were prepared for TEM analyses by the drop casting method using suspensions of  
36 WUI fire ash dispersed in methanol. The suspensions were shaken, left to sit for several minutes,  
37 and then dropped onto LC300-Cu-150 TEM grids (Electron Microscopy Sciences), which consist  
38 of a lacey carbon support layer attached to a 300-mesh copper grid. The TEM samples were stored  
39 in a vacuum desiccator before being analyzed. TEM data were collected at the Nanoscale  
40 Characterization and Fabrication Laboratory at Virginia Polytechnic Institute and State University  
41 on a JEOL JEM 2100 S/TEM, operated at 200 kV. TEM bright field images were acquired with a  
42 Gatan Ultrascan 1000XP CCD camera, whereas selected area electron diffraction patterns were  
43 collected with a Gatan Orius 833 slow scan CCD camera. Energy dispersive X-ray spectroscopy  
44  
45  
46  
47  
48  
49  
50  
51  
52  
53  
54  
55  
56  
57  
58  
59  
60

(EDS) elemental maps were obtained using a JEOL genuine 60 mm<sup>2</sup> Silicon Drift Detector. For NP phase identification, we used a combination of compositional information from EDS analyses as well as electron diffraction data. For NPs >200 nm, we used selected area electron diffraction, but for smaller NPs or those overlapping with adjacent material to a significant extent, we ran fast-Fourier-transforms (FFTs) on high-resolution TEM bright field images, a technique which generates diffraction patterns.

#### 2.4. X-ray absorption spectroscopy

X-ray Absorption Near Edge Structure (XANES) analyses were conducted at the Fe K-edge (7112 eV) on the P65 undulator beamline of the Deutsches Elektronen-Synchrotron (HASYLAB/DESY PetraIII, Hamburg, Germany)<sup>44</sup>. Incoming photon flux energy was modulated with a Si(111) double crystal monochromator, with an energy resolution of ~0.7 eV at the Fe K-edge, and a beam size of 0.3 x 1.5 mm<sup>2</sup>. The effective suppression of higher harmonics was achieved using Si-plane mirrors.

Around 100 mg of each ash sample was carefully ground, mixed with a small amount of cellulose, and pressed into a pellet. Given the relatively low Fe concentration in most of the ash samples, the absorption of the pellets was too high to obtain a transmission measurement of the reference Fe foil simultaneously to sample measurement. In this manner, Fe foil was measured several times over the course of the experiment to ensure a proper alignment. Over-absorption was corrected using the fluorescence correction module present in Larch<sup>45</sup>.

The data were collected from -150 eV below the edge to +700 eV above with a scan energy increment of ~0.4 eV in continuous mode, at room temperature. The time for each spectrum was 180 seconds and a total of 10 to 30 scans were averaged for each sample. Samples were measured in fluorescence mode. Model compounds were carefully ground with cellulose (2.5% iron), packed in ~1mm thick pellet with a pressure press, sealed with Kapton<sup>TM</sup> tape and kept inside a glovebox

1  
2  
3 until measurement for the model compounds sensitive to oxidation. Except for  $\text{Fe}_2(\text{SO}_4)_3$ , which  
4 is sensitive to reduction under the beam and was measured at 20K in a He-cryostat, all other model  
5 compounds were measured at room temperature, similar to the samples. Spectra were measured in  
6 transmission mode using ionization chambers with a path length of 5 cm filled with a mixture of  
7  $\text{N}_2$ , Ar, and Kr to obtain approximately 15, 50, and 100% absorption for the first, second, and third  
8 ionization chambers, respectively. Fe foil reference was measured simultaneously to the model  
9 compounds. For energy calibration and alignment, the first inflection point in the first derivative  
10 of the adsorption threshold of Fe foil was calibrated to 7112 eV.  
11  
12  
13  
14  
15  
16  
17  
18  
19  
20

21 Fe K-edge XAS spectra were calibrated, averaged, normalized, analyzed, fitted, and plotted  
22 using a series of in-house notebooks written in Python using the Larch<sup>45</sup> and Araucaria<sup>46</sup> libraries,  
23 Numpy<sup>47</sup>, SciPy<sup>48</sup> and Matplotlib<sup>49</sup>.  
24  
25  
26  
27

28 XANES was used to identify the Fe species present in ash. Least-square linear combination  
29 fitting (LCF) of the XANES region was performed over an energy range of -20 to +70 eV around  
30 7112 eV. The library of Fe model phases consisted of a mixture of commercial references (< 50  
31 nm  $\text{Fe}_2\text{O}_3$  nanopowder, FeS trace metal basis 99.9% purity,  $\text{Fe}(\text{NO}_3)_3 \cdot 9\text{H}_2\text{O}$ , trace metal basis,  
32 99.95% purity, FeO -10 mesh,  $\geq 99.6\%$  trace metals basis,  $\text{FeCl}_3$  sublime grade,  $\geq 99.9\%$  trace  
33 metal basis,  $\text{FeCl}_2$  tetrahydrate 99.99% trace metal basis) purchased from Aldrich. Model iron  
34 oxide compounds such as goethite, ferrihydrite, magnetite, maghemite and hematite were  
35 synthesized<sup>50,51</sup> as summarized in the SI section. The XANES spectra for all the model compounds  
36 used to fit the ash spectra are presented in **Figure S4**. The spectral weight of the iron oxide phases  
37 and oxidation states in the ashes are summarized in **Table S2**.  
38  
39  
40  
41  
42  
43  
44  
45  
46  
47  
48  
49  
50

51 To assess the collinearity between the spectra of the Fe model compounds library and to  
52 ensure a well-conditioned basis set for LCF, we used the condition number<sup>52,53</sup>. The chi-square  
53  
54  
55  
56  
57  
58  
59  
60

metric was used to estimate the goodness of the LCF analysis (**Table S2**). To include a reference in the fit, the amount of the model compounds must be superior to 10% and improve the quality of the fit by at least 20%. The uncertainties on the percentage of the distribution obtained by LCF were calculated using the Imfit library <sup>54</sup>.

### 3. Results

#### 3.1. Elemental Analysis

The total Fe concentration in the ash samples varied between 4 and 66 mg.g<sup>-1</sup>, except one ash (A092) which had a much higher Fe content of 321 mg.g<sup>-1</sup> (**Figure 2**). The median Fe concentration decreased in the following order: vegetation ash 36.1 mg g<sup>-1</sup> (range: 5.1 to 65.6 mg g<sup>-1</sup>) > soils 33.1 mg g<sup>-1</sup> (range: 19.2 to 48.5 mg g<sup>-1</sup>) > structural ash 18.5 mg g<sup>-1</sup> (range: 4.5 to 51.0 mg g<sup>-1</sup>) with one sampling having an exceptionally high Fe concentration of 321 mg g<sup>-1</sup> > vehicle 13.2 mg g<sup>-1</sup> (range: 4.6 to 43.3 mg g<sup>-1</sup>). Thus, the majority of iron entering the environment following fires likely originates from wildland fuels.

#### 3.2. Transmission electron microscopy analysis

Nanoparticles with various elemental compositions (*e.g.*, Cr, Cu, Fe, Ti) were identified in ash samples A122 and A124. Other metal/metal oxide NPs such as Zn- and Mn-bearing NPs were also identified in other ash samples but are not discussed here. Ash A122 contains Cr-, Cu-, Fe-, and Ti-bearing NPs. Their size (listed as the longest dimension for a particle) ranges are as follows: 180 to 270 nm (n = 3) for Cr-bearing NPs, 10 to 50 nm (n = 13) for Cu-bearing NPs, 190 to 270 nm (n = 2) for Fe-bearing NPs, and 40 to 250 nm (n = 18) for Ti-bearing NPs. Ash A124 contains Cr-, Fe-, and Ti-bearing NPs, with size ranges: 90 to 140 nm (n = 2) for Cr-bearing NPs, 280 to 1070 nm (n = 6) for Fe-bearing NPs, and 190 to 440 nm (n = 13) for Ti-bearing NPs. **Figure 3** shows an example of NPs observed in ash A124. The aggregate consists of an aluminum silicate, calcium carbonate, six Fe-bearing NPs, and thirteen Ti-bearing NPs. For the current study, we

1  
2  
3 focused on the mineral phase identification of the Fe-bearing NPs. Electron diffraction data on the  
4 Fe-bearing NPs in ash A124 are consistent with maghemite and/or magnetite. An example of a Fe-  
5 bearing NP with its associated diffraction data is shown in **Figure 4**. Measurements of the *d*-  
6 spacings values of the diffraction spots yielded 8.057, 4.041, 2.707, and 2.549 Å, corresponding  
7 to the (100), (200), (300), and (131) lattice planes of maghemite or magnetite. Maghemite and  
8 magnetite have very similar structures and interatomic distances, and thus, are often difficult to  
9 distinguish from each other by electron diffraction. However, maghemite is only composed of  
10 Fe<sup>3+</sup> whereas 1/3 of Fe in magnetite is Fe<sup>2+</sup>. Thus, it is possible to determine the presence of either  
11 magnetite or maghemite using XANES <sup>55</sup>.

### 23 24 **3.3. Bulk X-ray absorption near edge spectroscopy**

25  
26 The total bulk XANES of representative ash and soil samples are presented in **Figure 5a**.  
27 The bulk XAS spectra provide an estimate of the weighted atomic average of all major Fe species  
28 present in the sample at more than 10%. Spectra were dominated (*e.g.*, > 50%) by different Fe  
29 components such as ferrihydrite (amorphous hydrous ferric oxide), maghemite, magnetite,  
30 goethite ( $\alpha$ -Fe<sup>3+</sup>OOH), and hematite ( $\alpha$ -Fe<sup>3+</sup><sub>2</sub>O<sub>3</sub>, **Figure 5b**). Other phases such as FeCl<sub>3</sub>,  
31 Fe(NO<sub>3</sub>)<sub>3</sub>, Fe<sub>2</sub>(SO<sub>4</sub>)<sub>3</sub>, FeS, FeCl<sub>2</sub>, FeSO<sub>4</sub>, and metallic Fe (Fe<sup>0</sup>) occurred primarily as minor phases  
32 (*e.g.*, < 50%) in the ash samples. The combustion of vegetation and structural materials produces  
33 heat and emissions in the form of water, organic vapors, gases, and particulates. Gaseous emissions  
34 include carbon monoxide (CO), carbon dioxide (CO<sub>2</sub>), sulfur oxides (SO<sub>x</sub>), nitrogen oxides (NO<sub>x</sub>),  
35 and hydrogen chloride (HCl). These gases react with iron forming various iron compounds (*e.g.*,  
36 FeS, FeCl<sub>2</sub>, FeCl<sub>3</sub>, FeSO<sub>4</sub>, and Fe<sub>2</sub>(SO<sub>4</sub>)<sub>3</sub> as observed by XANES).

37  
38  
39  
40  
41  
42  
43  
44  
45  
46  
47  
48  
49  
50  
51  
52  
53  
54  
55  
56  
57  
58  
59  
60  
Maghemite and magnetite were the most frequently detected Fe phases in the ash samples  
(**Table 1**). Maghemite, ferrihydrite, goethite, hematite, FeCl<sub>3</sub>, and FeCl<sub>2</sub> were detected in fire ash  
as well as soil samples. In contrast, magnetite, FeS, FeSO<sub>4</sub>, Fe<sub>2</sub>(SO<sub>4</sub>)<sub>3</sub>, Fe(NO<sub>3</sub>)<sub>3</sub>, wüstite (FeO),

1  
2  
3 and Fe<sup>0</sup> were not detected in any of the five soil samples investigated in this study, suggesting that  
4 these phases formed due to material combustion in fires at the WUI. Sulfur-containing iron phases  
5 were not detected in any of the vegetation ash suggesting that these phases formed as a result of  
6 the combustion of sulfur-containing materials in structures and vehicles. Notably, these phases  
7 could be present in vegetation ash in small amounts. However, one of the intrinsic limitations of  
8 LCF is the error associated with this mathematical method and the resolution of the XANES  
9 spectra. It is commonly accepted in the XAS scientific community that species with mass below  
10 10% of sample mass do not strongly affect the shape of the fit, and thus cannot be considered as  
11 part of the sample <sup>56, 57</sup>.

12  
13  
14  
15  
16  
17  
18  
19  
20  
21  
22  
23  
24 Considering fire severity, indicated by ash color (**Figures 6, S5 and S6**), the majority of  
25 ash samples collected from low and medium burn-severity fires (11 out of 13 black ashes, 10 out  
26 of 11 gray ashes, and 5 out of 6 brown/gray ashes) contained magnetite. In contrast, a lower  
27 proportion of ashes collected from high burn-severity fires (10 out of 16 white ashes) contained  
28 magnetite (**Table 2**). Note that ash classification by color was performed by the naked eye, and  
29 that some of the white ashes contained light gray particles. This might explain why some white  
30 ashes contained magnetite. Considering the abundance of magnetite as a function of the color of  
31 the ash, we found that the relative abundance of magnetite decreased from black to gray to  
32 gray/brown to white to green ashes and was absent in red/brown ashes (**Figures 6a and S6a**).  
33 Conversely, the relative abundance of maghemite increased from black and gray to gray/brown  
34 and white to green, and red/brown (**Figures 6a and S6a**). In short, increasing fire severity was  
35 correlated with a decrease in magnetite and an increase in maghemite abundance. In addition, four  
36 gray ash samples contained wüstite, and three white ash samples contained metallic Fe. Comparing  
37 the iron oxidation states based on the ash color (**Figures 6b and S6b**), Fe<sup>3+</sup> increased from gray  
38  
39  
40  
41  
42  
43  
44  
45  
46  
47  
48  
49  
50  
51  
52  
53  
54  
55  
56  
57  
58  
59  
60



1  
2  
3 to black and gray/brown to white, green, and red/brown ashes (**Figure 6b**),  $\text{Fe}^{3+}/\text{Fe}^{2+}$  decreased  
4 following the same trend as magnetite (**Figure 6b**), and  $\text{Fe}^{2+}$  did not display a specific trend with  
5 ash color (**Figure 6b**). Iron speciation did not display a specific trend as a function of the ash  
6 source (**Figure S7**).  
7  
8  
9

10  
11  
12 The concentration of iron phases in the ashes was estimated using the total Fe concentration  
13 and the spectral weight obtained by LCF XANES assuming that the spectral weight of the different  
14 phases corresponds to the relative abundance of phase mass within the ashes (**Figure S6**). Most  
15 ash samples contained high magnetite levels (*e.g.*, up to 25 mg g<sup>-1</sup> in fire ash, 18 mg g<sup>-1</sup> in  
16 atmospherically deposited ash, **Figure 7**). Magnetite concentrations decreased from black to gray  
17 to white ash. These concentrations are much higher than those reported in roadside dust (*e.g.*, 1.8  
18 to 9.5 mg g<sup>-1</sup>)<sup>58</sup> or atmospheric particles (*e.g.*, 0.6 to 13.0 mg g<sup>-1</sup>)<sup>59-61</sup>. The concentration of wüstite  
19 varied between 2.4 and 23 mg g<sup>-1</sup>, whereas the concentration of metallic Fe varied between 0.9  
20 and 2.4 mg g<sup>-1</sup> (**Figure S8**). The concentrations of metallic Fe in road dust are relatively low (~  
21 0.15 mg g<sup>-1</sup>)<sup>58</sup>.  
22  
23  
24  
25  
26  
27  
28  
29  
30  
31  
32  
33  
34

35  
36 The relative abundance of the different oxidation states of Fe and the phases themselves in the  
37 WUI ash samples are presented in **Figures 6b and S6b**. The oxidized  $\text{Fe}^{3+}$  components were the  
38 dominant type in most ash samples and represented 0 to 100% of the total normalized Fe spectral  
39 signal (**Figure 6b**). The mixed  $\text{Fe}^{3+}/\text{Fe}^{2+}$  phases represented 0 to 81%, the reduced  $\text{Fe}^{2+}$   
40 represented 0 to 98%, and the most reduced  $\text{Fe}^0$  represented 0 to 14%. In contrast, in the soil  
41 samples, oxidized  $\text{Fe}^{3+}$  accounted for 77 to 100% and  $\text{Fe}^{2+}$  accounted for only 0 to 23% of the total  
42 normalized Fe spectral signal.  
43  
44  
45  
46  
47  
48  
49  
50  
51  
52  
53  
54  
55  
56  
57  
58  
59  
60

#### 4. Discussion

XANES analyses revealed that the dominant iron phases in the soil samples investigated in this study were ferrihydrite, goethite, maghemite, hematite,  $\text{FeCl}_2$ , and  $\text{FeCl}_3$ . Iron oxyhydroxides such as ferrihydrite, goethite, lepidocrocite ( $\gamma\text{-Fe}^{3+}\text{OOH}$ ), and hematite were the major forms of iron in soils as products of weathering reactions of the soil parent <sup>62</sup>. In contrast, vegetation, structure, and vehicle ashes were dominated by ferromagnetic (*i.e.*, magnetically ordered) minerals, especially magnetite and maghemite. Other Fe-bearing phases were also detected in these ashes, including hematite, wüstite, and metallic Fe. These findings suggest that magnetite, wüstite, and metallic Fe formed due to the combustion of materials during fires at the WUI.

Iron oxide NPs undergo various transformations during material combustion, which depend on the fire redox conditions. For instance, hematite is resistant to transformation at high temperature under oxidizing conditions. In contrast, under reducing conditions, hematite can be converted to maghemite or magnetite. Heat treatment of hematite and goethite in the presence of a reducing agent (5 wt.% starch,  $(\text{C}_6\text{H}_{10}\text{O}_5)_n$ ) leads to their conversion into magnetite. This transformation starts at 300 to 350 °C and increases with temperature <sup>63-65</sup>, then the transformation rate decelerates at approximately 500 °C <sup>63</sup>. Hematite transforms to maghemite or magnetite in the presence of organic matter at temperatures > 450 °C <sup>66</sup>. This transformation is caused by the partial reduction of  $\text{Fe}^{3+}$  to  $\text{Fe}^{2+}$  by carbon and the subsequent formation of maghemite and magnetite. Thermal treatment of lepidocrocite under oxidizing conditions leads to the formation of maghemite at 250 °C, which then starts to transform to hematite at 350 °C. In contrast, thermal treatment of lepidocrocite under reducing conditions leads to the formation of magnetite through the intermediate formation of maghemite and hematite. These transformations start at 200 to 250°C

1  
2  
3 and continue up to 900 °C<sup>67, 68</sup>. When heated under oxidizing conditions, goethite transforms to  
4 hematite. In contrast, when heated under reducing conditions, goethite (natural coarse particles of  
5 goethite iron ore) transforms to magnetite with possible intermediate hematite formation<sup>2, 69-71</sup>. In  
6 the presence of glucose, goethite begins to transform to a high-magnetic mineral at 450 °C<sup>66</sup>. The  
7 reduction of synthetic and brown goethite results in the formation of magnetite at 270 °C and 500  
8 °C, respectively<sup>72</sup>. Therefore, temperature and redox conditions are expected to be the most  
9 important factors controlling the transformations of iron oxides in the case of fire events in the  
10 WUI.  
11  
12  
13  
14  
15  
16  
17  
18  
19  
20

21 The pyrolysis of biomass (*e.g.*, pine tree biomass, palm oil waste) and structural material  
22 (*e.g.*, wood) generates heat, CO, H<sub>2</sub>, and black carbon, which act as heating and reducing agents  
23 for the reduction of iron oxide<sup>2, 3</sup>. The CO, H<sub>2</sub>, and black carbon reductants cause the reduction  
24 process through a series of interrelated reactions (Eq. 1-6)<sup>73, 74</sup>. The complete reduction of iron  
25 oxides consists of the reduction of iron oxides (*e.g.*, hematite, goethite, lepidocrocite) to magnetite,  
26 magnetite to wüstite, and wüstite to metallic iron. The degree of iron oxide reduction is determined  
27 by the reduction temperature, reaction time, and air/biomass ratio<sup>2</sup>.  
28  
29  
30  
31  
32  
33  
34  
35  
36



37  
38  
39  
40  
41  
42  
43  
44  
45  
46  
47  
48  
49  
50  
51 Depending on the availability of excess carbon and hydrogen, the reduction follows the  
52 above stepwise mechanism during fires at the WUI. Increases in reduction temperature, reaction  
53  
54  
55  
56  
57  
58  
59  
60

1  
2  
3 time, the concentration of the reducing agent (*e.g.*, CO, H<sub>2</sub>, black carbon), as well as the decrease  
4  
5 in iron oxide particle size favor the reduction of iron oxides (*e.g.*, goethite, hematite, lepidocrocite)  
6  
7 to magnetite, wüstite, and finally metallic iron<sup>63, 73</sup>.  
8  
9

10 The lower relative abundance of magnetite in white ashes (*e.g.*, high-fire severity) could  
11  
12 be due to (i) the transformation of magnetite to the more reduced iron oxide phases at higher fire  
13  
14 severity, which is supported by the detection of wüstite in gray ashes and Fe<sup>0</sup> in white ashes (**Table**  
15  
16 **2**); (ii) the decrease in the reducing agent (electron acceptor) concentrations under high-fire  
17  
18 severity conditions; and/or (iii) the oxidative transformations of reduced iron phases to the  
19  
20 oxidized forms (*e.g.*, maghemite and hematite) due to a change in the environmental redox  
21  
22 conditions. Under low-fire severity (*i.e.*, < 450 °C) conditions, carbon is not completely oxidized,  
23  
24 which generates CO and/or black carbon. In contrast, high intensity fires (> 450 °C) produce CO<sub>2</sub>,  
25  
26 H<sub>2</sub>O, and light gray or white ashes composed of mainly alkaline oxides (Ca, K, Mg oxides)<sup>75</sup>. The  
27  
28 total amount and duration of CO emissions decrease with increases in combustion temperature due  
29  
30 to increased combustion completeness<sup>76</sup>. Additionally, the amount of emitted CO and black  
31  
32 carbon depends on the type of burned biomass or structural material. These conditions might limit  
33  
34 the reduction of iron oxides under high-fire severity. On the other hand, newly formed magnetite  
35  
36 (by reduction of hematite in the presence of starch or other organic matter) could re-oxidize to  
37  
38 maghemite at temperatures > 600 °C due to changes in reducing and oxidizing conditions (*i.e.*,  
39  
40 consumption of starch during the reduction reaction)<sup>2, 63, 77</sup>. In contrast, at low fire severity black  
41  
42 carbon could prevent the reoxidation of reduced iron oxides<sup>78</sup>.  
43  
44  
45  
46  
47  
48

## 49 **5. Implications for public health and global warming**

50  
51 This study reveals that wildfires at the WUI can convert iron oxides to reduced iron phases  
52  
53 such as magnetite, wüstite, and zero-valent iron. We found that magnetite concentrations (up to 25  
54  
55  
56  
57  
58  
59  
60

1  
2  
3 mg g<sup>-1</sup> of ash) in deposited and atmospherically transported ash are higher than those reported in  
4  
5 typical atmospheric and roadside particles. These findings provide important information for  
6  
7 understanding the potential health risks, environmental impacts, and global warming implications  
8  
9 of wildfires at the WUI, all of which remain poorly understood.  
10

11  
12 In terms of public health risks, wildfires, wood smoke, and magnetite exposures have been  
13  
14 associated with neurodegenerative diseases such as cognitive dysfunction, including Alzheimer's  
15  
16 disease and dementia <sup>17, 18, 35, 36, 79</sup>. Considering the potential neurotoxicity of magnetite particles  
17  
18 and the abundance of magnetite NPs in wildfire emissions, it is reasonable to speculate that  
19  
20 magnetite particles emitted from fires at the WUI could contribute to the pathogenesis of  
21  
22 neurodegenerative diseases, warranting further investigation. This is of particular concern for the  
23  
24 entire population of the continental United States and many other countries due to the long-  
25  
26 distance transport and related, widespread exposure to wildfire contaminants.  
27  
28  
29

30  
31 Wildfire smoke is a major source of ambient particulate matter, contributing to as much as  
32  
33 70% of PM<sub>2.5</sub> in the western United States on days when regulatory limits (10 µg.m<sup>-3</sup>) are exceeded  
34  
35 <sup>80</sup>. PM<sub>2.5</sub> refers to particulate pollutants that are 2.5 micrometers or smaller in size and are  
36  
37 associated with the greatest proportion of adverse health effects related to air pollution, including  
38  
39 premature mortality, increased hospital admission for heart or lung causes, acute and chronic  
40  
41 bronchitis, asthma attacks, emergency room visits, respiratory symptoms, and restricted activity  
42  
43 days <sup>81</sup>. The North American annual PM<sub>2.5</sub> emissions from wildfires are estimated at 1.9 to 2.2  
44  
45 Tg/year <sup>82</sup>, and the total U.S. anthropogenic PM<sub>2.5</sub> emissions are estimated at 4.1 Tg/year <sup>83</sup>. A  
46  
47 multi-year (2013-2016) analysis of wildfire forecasted PM<sub>2.5</sub> concentrations from burning biomass  
48  
49 over North America suggested that on average over the fire season, 69% of United States residents  
50  
51 and 76% of Canadian residents were affected by seasonal wildfire-related PM<sub>2.5</sub> concentrations  
52  
53  
54  
55  
56  
57  
58  
59  
60

1  
2  
3 above  $0.2 \mu\text{g.m}^{-3}$ , and these effects were particularly pronounced in July and August <sup>84</sup>.  
4  
5 Additionally, fire emissions contributed more than  $1 \mu\text{g.m}^{-3}$  of daily average  $\text{PM}_{2.5}$  concentrations  
6  
7 on more than 30% of days in the western United States and northwestern Canada during the fire  
8  
9 season <sup>84</sup>. The  $0.2 \mu\text{g.m}^{-3}$  threshold is the threshold above which any annual  $\text{PM}_{2.5}$  change is  
10  
11 considered a non-negligible impact according to the U.S. Environmental Protection Agency (EPA)  
12  
13 Significant Impact Level. The  $1 \mu\text{g.m}^{-3}$  threshold is considered a transition between the minimal  
14  
15  $0.2 \mu\text{g.m}^{-3}$  and the  $10 \mu\text{g.m}^{-3}$  threshold <sup>85</sup>. The United States population affected by average  
16  
17 seasonal fire- $\text{PM}_{2.5} > 10 \mu\text{g.m}^{-3}$  ranged from 179,841 to 354,050, with a four-year season average  
18  
19 (2013-2016) exposure of 0.1% of the United States population <sup>84</sup>. It is expected that wildfire smoke  
20  
21 could generate greater than 50% of total  $\text{PM}_{2.5}$  for the entire United States by the year 2100 <sup>86</sup>. In  
22  
23 the present study, unraveling the abundances and properties of magnetite NPs provides a valuable  
24  
25 reference for toxicological studies and risk assessment.  
26  
27  
28  
29

30  
31 In terms of global environmental impacts, a recent study reported anomalously widespread  
32  
33 phytoplankton blooms in the Southern Ocean downwind of Australia. These blooms were  
34  
35 attributed to the transport of wildfire-generated iron-rich aerosols to the bloom regions, resulting  
36  
37 in the fertilization of the iron-limited waters of the Southern Ocean <sup>37</sup>, possibly due to the higher  
38  
39 solubility of iron in seawater from combustion sources than that from mineral dust <sup>87</sup>. Yet the role  
40  
41 of iron solid phase speciation and mineralogy have not yet been considered. The high relative  
42  
43 abundance of  $\text{Fe}^{2+}$  in fire ashes could play an important role in the bioavailability of iron in the  
44  
45 ocean <sup>38</sup>.  
46  
47  
48

49 In terms of global warming, particulate matter (*e.g.*, black carbon, brown carbon, and mineral  
50  
51 dust) has been largely considered as the only significant anthropogenic contributor to shortwave  
52  
53 (*e.g.*, 300 to 2500 nm) atmospheric heating <sup>88</sup>. However, anthropogenic iron oxide aerosols have  
54  
55  
56  
57  
58  
59  
60

1  
2  
3 been recently recognized to be significant contributors to shortwave atmospheric heating because  
4 iron oxides are strong absorbers at visible wavelengths<sup>39, 89</sup>. Iron speciation regulates the light-  
5 absorption properties of iron oxides. Magnetite is the most efficient shortwave absorber among the  
6 iron oxide minerals in the atmosphere, as the imaginary part of the refractive index for magnetite  
7 is similar to that of black carbon<sup>90, 91</sup>. The shortwave heating rates by anthropogenic magnetite  
8 particles, released from blast furnaces of iron manufacturing facilities and engine and brakes of  
9 motor vehicles, were estimated to be at least 4-7, 0.8-7, 0.7-14, and 0.3-26% of that of black carbon  
10 in East Asia, the Southern Ocean, the Pacific Ocean, and the Atlantic Ocean, respectively<sup>39, 92</sup>.  
11 Given their high concentrations, WUI fire-released magnetite may have a climate heating effect  
12 through absorption of shortwave solar radiation<sup>40</sup>. We note the discussion above provides only a  
13 brief discussion of the global environmental and climatological impacts of iron oxide nanoparticles  
14 in fire ashes. A more detailed discussion of the environmental and climatological impacts of iron  
15 oxide nanoparticles can be found elsewhere<sup>6</sup>.

16  
17  
18  
19  
20  
21  
22  
23  
24  
25  
26  
27  
28  
29  
30  
31  
32  
33 Our XANES analyses revealed that strongly magnetic particles (magnetite and maghemite)  
34 displayed a higher relative abundance (*e.g.*, 15 to 100% with an average of  $65\% \pm 23$  spectral  
35 weight) in fire ash relative to those in soils (*e.g.*, 16 to 43% with an average of  $29\% \pm 10$  spectral  
36 weight). These findings suggest that wildfires contribute to the magnetic enhancement of topsoil  
37 as reported elsewhere<sup>29, 93</sup>. Understanding the impact of fires on soil magnetism is important for  
38 accurate interpretation of magnetic paleoenvironmental proxies.

39  
40  
41  
42  
43  
44  
45  
46  
47 This study focused on the speciation of Fe-bearing particles in WUI fire ashes. Future studies  
48 investigating the solid phase speciation of other metal-bearing particles such as Ti, Cr, and Cu-  
49 bearing particles could provide additional valuable insights.

## 6. Acknowledgements

This work was supported by a RAPID grant (2101983) from the United States National Science Foundation (NSF) and by the Nanoscale Characterization and Fabrication Laboratory and the Virginia Tech National Center for Earth and Environmental Nanotechnology Infrastructure (NanoEarth), a member of the National Nanotechnology Coordinated Infrastructure (NNCI), supported by NSF (ECCS 1542100 and ECCS 2025151). We acknowledge DESY (Hamburg, Germany), a member of the Helmholtz Association HGF, for the provision of experimental facilities. Parts of this research were carried out at PetraIII, and we would like to thank Edmund Welter and Regina Biller for their assistance in using the beamline P65. We would like to thank Thaïs Couasnon, Jeff P. Perez and Roberts Blukis from the GFZ German Research Center for Geosciences as well as Akhil Tayal and Xiao Sun from DESY, for providing some of the Fe references for XAS analysis and helping with the synthesis of others. Any use of trade, firm, or product names is for descriptive purposes only and does not imply endorsement by the U.S. Government.

### 1. Competing interest statement

The authors declare no competing interest.

### 2. Author Contributions

Dr. Mohammed Baalousha conceived the overall idea of the research, coordinated the collaboration among the research team, performed data analysis, and wrote the first draft. Dr. Jackson P. Webster, Dr. Sandrine J. Matiasek, and Dr. Charles N. Alpers performed field sampling campaigns and provided extensive background information on the sampling sites and the collected samples. Dr. Morgane Desmau collected the X-ray absorption data and performed data analysis. Dr. Sheri Singerling performed transmission electron microscopy analysis and the associated data



1  
2  
3 analysis. Dr. Michelle A. Stern generated the burn severity and land use maps. All authors  
4  
5 contributed to the manuscript writing and editing.  
6  
7  
8  
9  
10  
11  
12  
13  
14  
15  
16  
17  
18  
19  
20  
21  
22  
23  
24  
25  
26  
27  
28  
29  
30  
31  
32  
33  
34  
35  
36  
37  
38  
39  
40  
41  
42  
43  
44  
45  
46  
47  
48  
49  
50  
51  
52  
53  
54  
55  
56  
57  
58  
59  
60

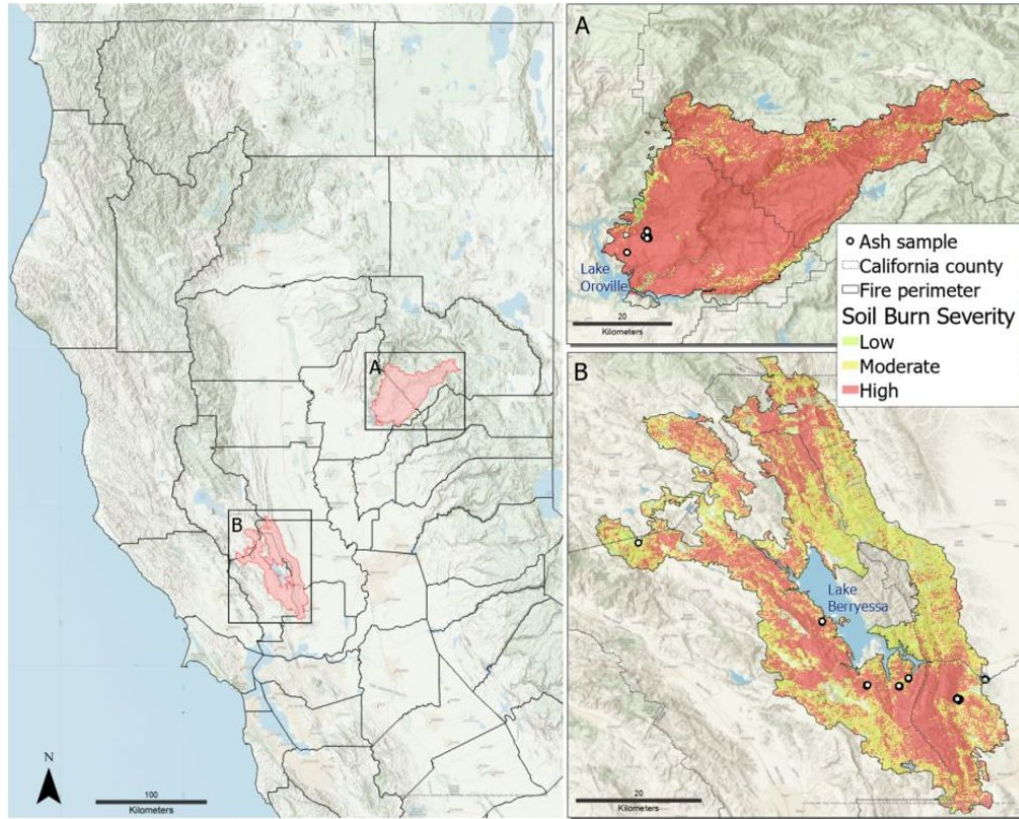


**Figure 1.** Map of soil burn severity in the two fires investigated in this study (A) the North Complex (NC) and (B) the LNU Lightning Complex.

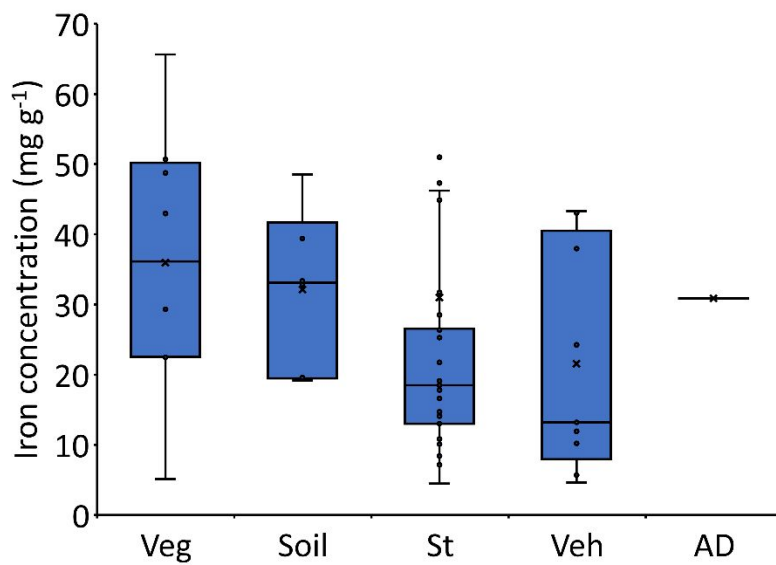


**Figure 2.** Total iron concentration in wildland-urban interface ash. Veg: vegetation, St: structure, Veh: vehicle, and AD: atmospheric deposition.

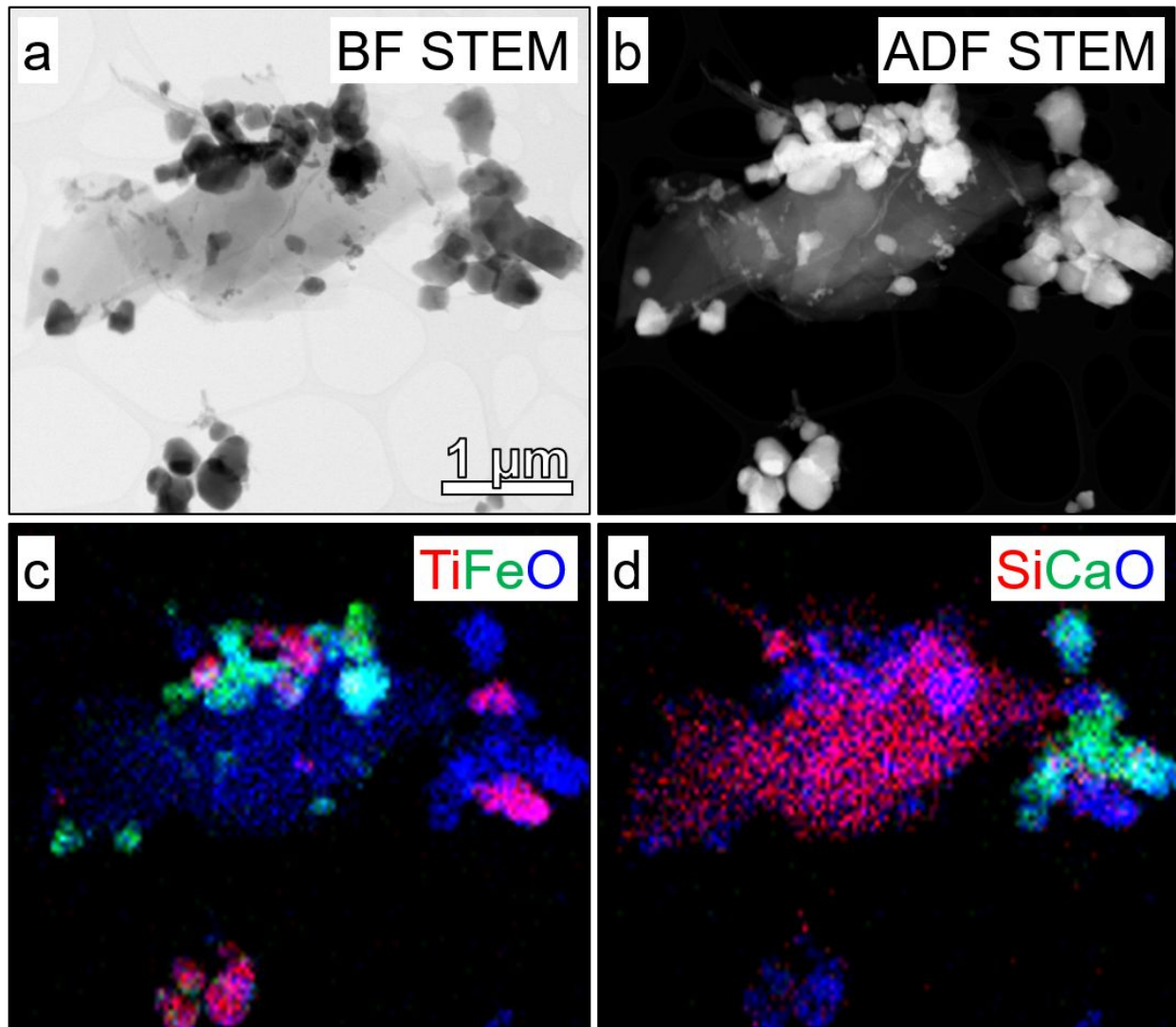


**Figure 3.** TEM images and EDS maps illustrating maghemite/magnetite nanoparticles in an aggregate from ash A124. The aggregate's overall morphology is shown in (a) bright field (BF) and (b) annular dark field (ADF) scanning TEM images, whereas compositional information is presented in two composite EDS maps—(c) Ti in red, Fe in green, and O in blue and (d) Si in red, Ca in green, and O in blue.

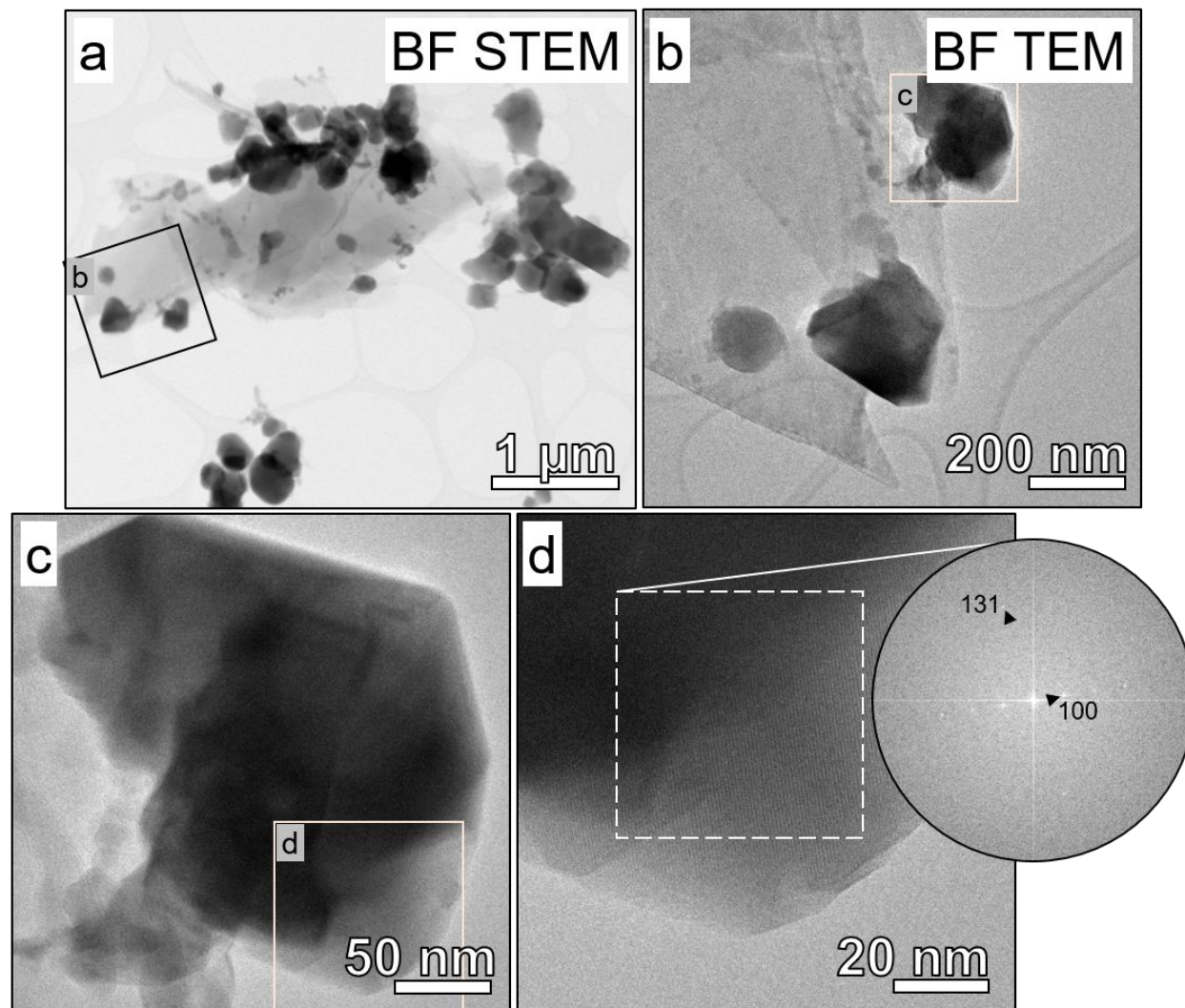


**Figure 4.** TEM images and an electron diffraction pattern from maghemite/magnetite nanoparticles in an aggregate from ash A124. The images are shown in increasing magnification with the location of the higher magnification images included as insets. A high-resolution bright field (BF) TEM image is shown in (d) with lattice fringes visible. An FFT was performed on the region outlined in white, with the resulting electron diffraction pattern included. It matches [013] for both magnetite and maghemite.

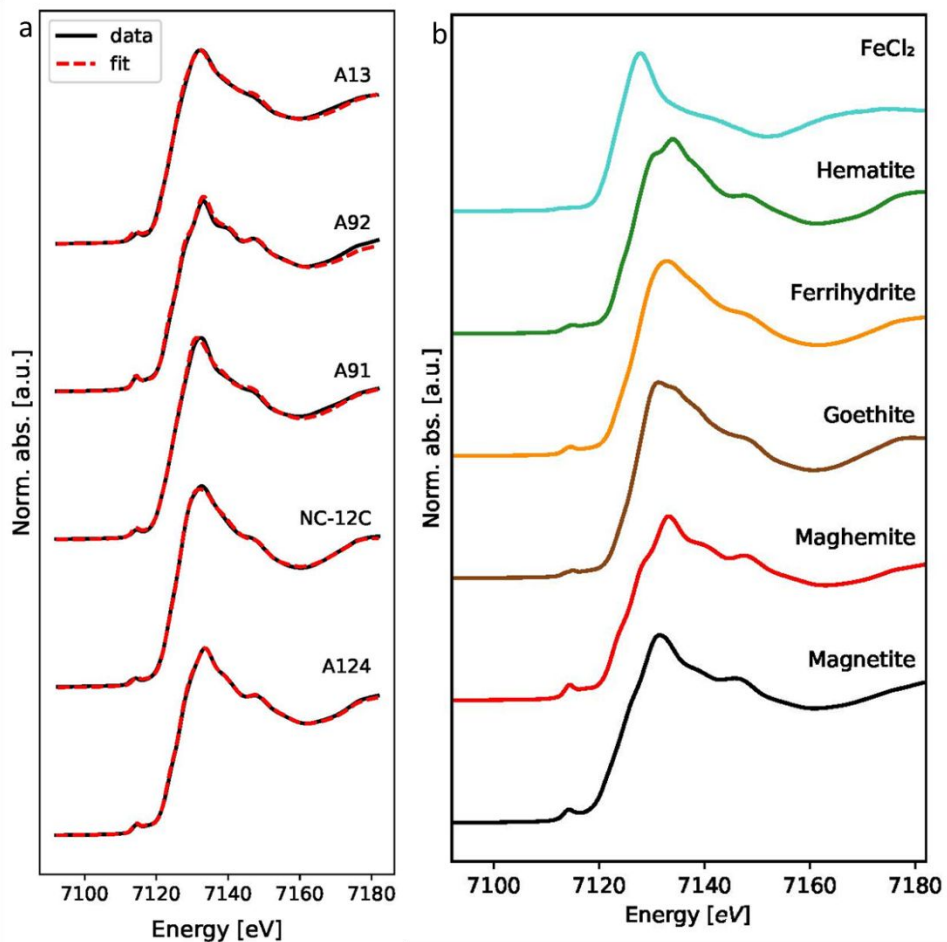


**Figure 5.** Example of iron K-edge XANES spectra of (a) fire ash samples and their linear combination (LC) best fits, and (b) the model compounds present in the selected ashes. The ash samples include A124: a structural gray ash, NC-12C: a soil red ash, A091, a structural red ash, A092, a structural black ash, and A013: a structural black ash.

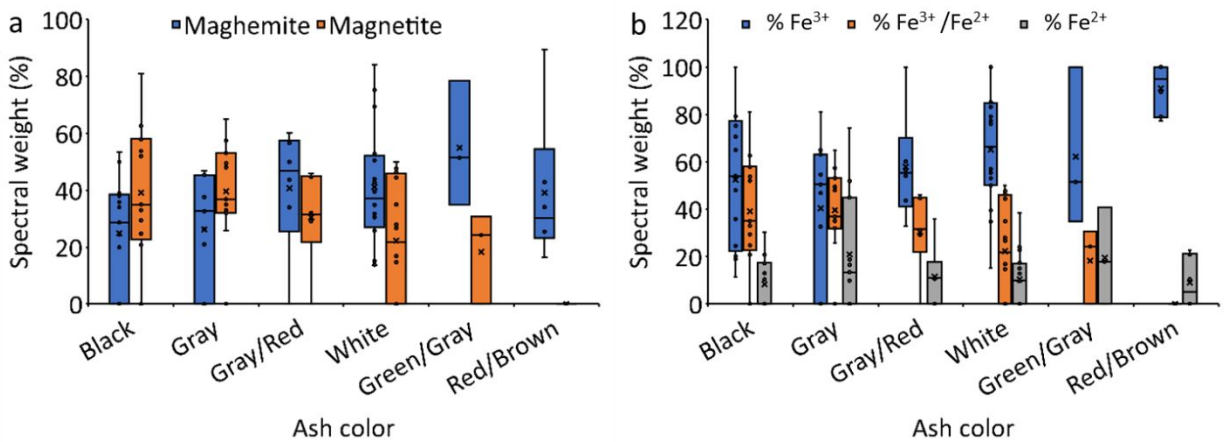


**Figure 6.** The spectral weight (%) of (a) magnetite and maghemite, and (b) iron oxidation state in ash and soil samples organized by ash color.

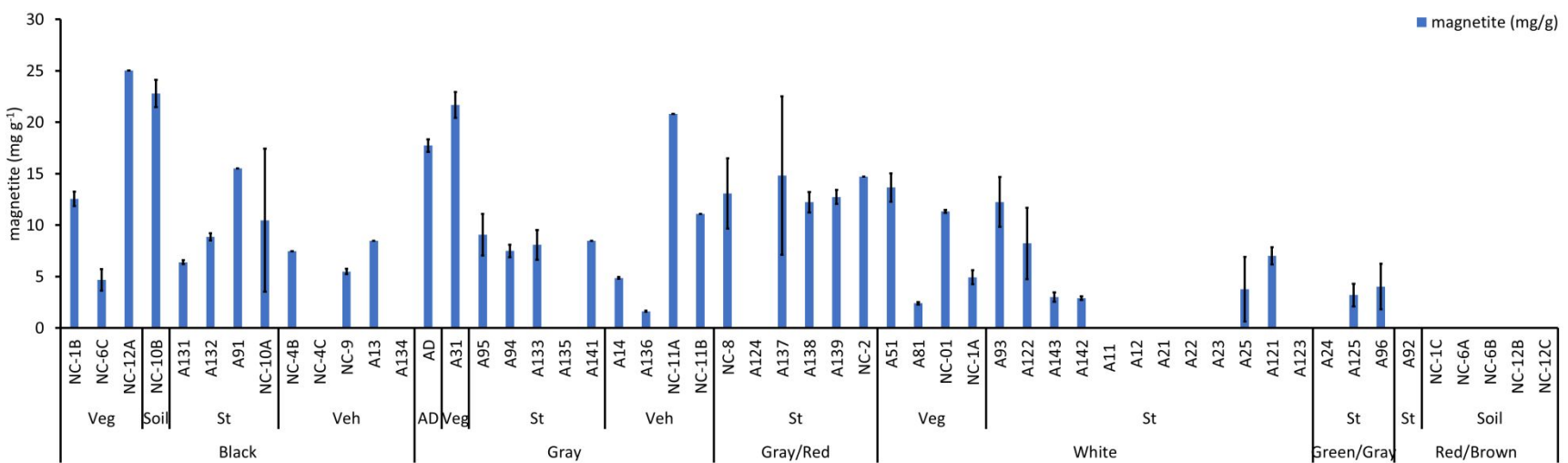


**Figure 7.** Magnetite concentration (mg g<sup>-1</sup>) in ash generated as a result of fires at the wildland-urban interface as a function of ash color and fuel source. Veg: vegetation, St: structure, Veh: vehicle, and AD: atmospheric deposition.



**Table 1.** Number of ash and soil samples containing a given phase based on ash source

Phase	All ash	Structural ash	Vegetation ash	Vehicle ash	Atmospheric deposition	Soil
Maghemite	42	30	6	5	1	5
Magnetite	38	23	7	7	0	0
Ferrihydrite	15	10	2	3	1	2
FeS	12	8	0	4	0	0
FeCl <sub>2</sub>	11	7	3	1	0	2
FeSO <sub>4</sub>	11	9	0	1	1	0
Goethite	8	5	1	2	0	2
FeCl <sub>3</sub>	8	4	2	2	0	3
Hematite	5	2	2	1	0	3
Wüstite (FeO)	4	2	0	2	0	0
Fe <sup>0</sup>	3	3	0	0	0	0
Fe(NO <sub>3</sub> ) <sub>3</sub>	1	0	1	0	0	0
Fe <sub>2</sub> (SO <sub>4</sub> ) <sub>3</sub>	1	1	0	0	0	0

**Table 2.** Number of ash samples containing a given phase based on ash color

Phase	Black	Gray	Gray/Brown	White	Gray/Green	Red
Total number of ashes	13	11	6	16	3	6
Maghemite	9	8	5	16	3	6
Magnetite	11	10	5	10	2	0
Ferrihydrite	5	3	1	6	0	2
FeS	2	4	0	5	1	0
FeCl <sub>2</sub>	2	2	1	5	0	3
FeSO <sub>4</sub>	2	3	3	2	1	0
Goethite	3	2	1	2	0	2
FeCl <sub>3</sub>	2	2	0	3	1	3
Hematite	3	0	1	1	0	3
Wüstite (FeO)	0	2	1	0	1	0
Fe <sup>0</sup>	0	0	0	3	0	0
Fe(NO <sub>3</sub> ) <sub>3</sub>	1	0	0	0	0	0
Fe <sub>2</sub> (SO <sub>4</sub> ) <sub>3</sub>	0	0	0	1	0	0